Overcoming Charge Confinement in Perovskite Nanocrystal Solar Cells

Wenqiang Yang, Seung-Hyeon Jo, Yipeng Tang, Jumi Park, Su Geun Ji, Seong Ho Cho, Yongseok Hong, Dong-Hyeok Kim, Jinwoo Park, Eojin Yoon, Huanyu Zhou, Seung-Je Woo, Hyeran Kim, Hyung Joong Yun, Yun Seog Lee, Jin Young Kim, Bin Hu, and Tae-Woo Lee*

The small nanoparticle size and long-chain ligands in colloidal metal halide perovskite quantum dots (PeQDs) cause charge confinement, which impedes exciton dissociation and carrier extraction in PeQD solar cells, so they have low short-circuit current density J_{sc}, which impedes further increases in their power conversion efficiency (PCE). Here, a re-assembling process (RP) is developed for perovskite nanocrystalline (PeNC) films made of colloidal perovskite nanocrystals to increase J_{sc} in PeNC solar cells. The RP of PeNC films increases their crystallite size and eliminates long-chain ligands, and thereby overcomes the charge confinement in PeNC films. These changes facilitate exciton dissociation and increase carrier extraction in PeNC solar cells. By use of this method, the gradient-bandgap PeNC solar cells achieve a $J_{sc} = 19.30$ mA cm^{-2} without compromising the photovoltage, and yield a high PCE of 16.46% with negligible hysteresis and good stability. This work provides a new strategy to process PeNC films and pave the way for high performance PeNC optoelectronic devices.

1. Introduction

Colloidal metal halide perovskite quantum dots (PeQDs) have low defect density, slow hot-carrier cooling process, tunable bandgap, high absorption coefficient, uniform large-scale fabrication, and low cost, and therefore have great potential for use in new-generation photovoltaic technology.[1–5] The power conversion efficiency (PCE) of PeQD solar cells has been increased to surpass those of other quantum-dot solar cells.[6–8] Furthermore, PeQDs are more photostable than polycrystalline perovskites; this trait is crucial for long-term stability of solar cells.[9] However, PeQD solar cells have lower record PCEs than that of polycrystalline perovskite solar cells.[10]

The primary reason for the relatively low PCEs of PeQD solar cells is their lower short-circuit current density (J_{sc}) than those of polycrystalline perovskite solar cells. Perovskite nanocrystals include PeQDs under quantum confinement and nanoparticles beyond quantum confinement. When PeQDs or perovskite nanocrystals are assembled into a compact film, they lose long-chain ligands, and therefore tend to fuse together, so crystallite sizes typically exceed the exciton Bohr diameter. Considering this trend, we refer to films assembled from PeQDS or perovskite nanocrystals as perovskite nanocrystalline (PeNC) films. However, the PeNC films still have some degree of charge confinement due to their small crystallite size and residual long-chain ligands.[11,12] This

W. Yang, S.-H. Jo, S. G. Ji, D.-H. Kim, J. Park, E. Yoon, H. Zhou, S.-J. Woo, J. Y. Kim, T.-W. Lee
Department of Materials Science and Engineering
Seoul National University
1 Gwanak-ro, Gwanak-gu, Seoul 08826, Republic of Korea
E-mail: twlees@snu.ac.kr
W. Yang, T.-W. Lee
Research Institute of Advanced Materials
Seoul National University
1 Gwanak-ro, Gwanak-gu, Seoul 08826, Republic of Korea
Y. Tang, B. Hu
Department of Materials Science and Engineering
University of Tennessee
1001–1099 Estabrook Rd, Knoxville, TN 37996, USA

J. Park, Y. Hong
Department of Chemistry
Yonsei University
50 Yonsei-ro, Seodaemun-gu, Seoul 03722, Republic of Korea
S. H. Cho, Y. S. Lee
Department of Mechanical Engineering
Seoul National University
1 Gwanak-ro, Gwanak-gu, Seoul 08826, Republic of Korea
H. Kim, H. J. Yun
Advanced Nano Research Group
Korea Basic Science Institute (KBSI)
169-148 Gwahak-ro, Yuseong-gu, Daejeon 34126, Republic of Korea
T.-W. Lee
SN Display Co. Ltd.
1 Gwanak-ro, Gwanak-gu, Seoul 08826, Republic of Korea
T.-W. Lee
School of Chemical and Biological Engineering
Institute of Engineering Research, Soft Foundry
Seoul National University
1 Gwanak-ro, Gwanak-gu, Seoul 08826, Republic of Korea

charge-confinement hampers exciton dissociation and carrier extraction in PeNC films, and is therefore a major obstacle to increase the J_{sc}.

However, most reports about PeNC solar cells have only considered ways to optimize the ligand exchange method; few have considered the charge confinement in PeNC films and its influence on the PCEs of PeNC solar cells. Compared to polycrystalline perovskite films, PeNC films typically have higher exciton binding energy (E_b) due to the charge-confinement effect, and this high E_b degrades photovoltaic performances.[13] The high E_b impedes exciton dissociation and reduces the number of free carriers that can be converted to photocurrents, and thereby decreases the J_{sc} of PeNC solar cells. Further, although some reported ligand-exchange methods use short cations (e.g., formamidinium iodide (FAI), potassium iodide) dissolved in ethyl acetate (EtOAc) to replace the long-chain ligands, these short cations in EtOAc must compete with long-chain ligands that have anchored to the surface of colloidal perovskite nanocrystals in the solid film state. Moreover, these short cations have poor solubility in EtOAc and therefore reach very low concentration in EtOAc.[14,15] Consequently, the conventional method cannot effectively remove long-chain ligands, and can even generate additional formamidinium (FA) vacancies and halide vacancies due to their low formation energy.[16] As a result, the charge confinement in the PeNC films continues to inhibit the increase of J_{sc} in PeNC solar cells. Thus, to further increase the J_{sc} and PCE of PeNC solar cells, the charge confinement in the PeNC films must be overcome in a way that simultaneously increases crystallite size and eliminates long-chain ligands in PeNC films.

Here, we developed a simple re-assembling process (RP) for PeNC films made of colloidal perovskite nanocrystals. This process overcomes the charge confinement in the PeNC films by increasing the crystallite size and efficiently removing long-chain ligands. RP to post-treat the PeNC films was performed using a pyridine/2-isopropanol (IPA) mixture that contains FAI. In this process, pyridine can loosen the contact between long-chain ligands and the surface of colloidal perovskite nanocrystals, and then IPA washes away the residual long-chain ligands, and therefore enabling re-assemble PeNC films to obtain a larger crystallite size. The weakened charge confinement in the PeNC film was confirmed by the reduced E_b and improved carrier transport. Use of the photoexcitation-polarization-dependent photoluminescence (PL) and the bias-dependent magnetic field effects of PL to investigate the exciton behavior revealed that our strategy enabled the exciton–exciton interaction by spin scattering between orbital magnetic dipoles, and demonstrated a reduced E_b and facilitated exciton dissociation in the PeNC films. In addition, tracking of carrier transport in the PeNC films demonstrated an improvement in carrier extraction by use of our method. Moreover, the reduced defect density suggested that our method could provide robust passivation for the PeNC films. We also developed a gradient-bandgap structure of the PeNC films by using a layer-by-layer film formation technique utilizing colloidal perovskite nanocrystal that had various bandgaps. Consequently, use of RP in Cs/FA-mixed PeNC solar cells with our gradient bandgap structure achieved a notably high $J_{sc} = 19.30$ mA cm^{-2}, a high PCE = 16.46%, and negligible hysteresis. Compared to the conventional strategy, this new strategy can concurrently accelerate

exciton dissociation and improve carrier extraction by overcoming charge confinement in PeNC films.

2. Results and Discussion

To achieve high PCEs, we used PeNC films that have a gradient-bandgap structure, which can be obtained by spin-coating different-bandgap colloidal perovskite nanocrystals layer-by-layer, and which is beneficial to obtain high PCE.[17,18] To obtain this structure, we synthesized three different bandgap colloidal perovskite nanocrystals whose bandgaps were ≈1.72 eV, 1.65 eV, and 1.61 eV from wide to narrow respectively (Experimental Section and Figure S1, Supporting Information). These three-kind colloidal perovskite nanocrystals were spin-coated layer-by-layer in sequence (**Figure 1**a). The band positions of each layer and the energy band diagram for the gradient bandgap PeNC films were presented in the Figure S2 (Supporting Information).

After obtaining PeNC films with a desired thickness, RP samples were obtained by using the RP method, by which the PeNC films were post-treated using a mixture of pyridine and IPA that contain FA$^+$ as short cations, and control samples were obtained by using the conventional method to post-treat the PeNC films using ethyl acetate (EtOAc) with FA$^+$ as short cations to exchange long-chain ligands (Experimental Section).

We compared the device performance of solar cells fabricated using gradient-bandgap PeNC films with those using planar-bandgap PeNC films, both of which had been post-treated by either the control method or the RP method (Table S1, Supporting Information). The RP method effectively improved the PCEs of both planar-bandgap and gradient-bandgap devices. Furthermore, PCEs were higher in the solar cells that used gradient-bandgap PeNC films than in solar cells that used planar-bandgap PeNC films, irrespective of the post-treatment method. Thus, herein, we present results of only the gradient-bandgap PeNC films to investigate the difference between the control method and RP method. We carefully optimized the volume ratio of IPA to pyridine, the concentration of FAI in IPA, and the post-annealing temperature (Tables S2–S4, Supporting Information).

For the RP devices, the average PCE for the reverse and forward scan was increased to 16.46%, with a champion PCE = 16.68% under the reverse scan (Table S5, Supporting Information). However, the average PCE for the reverse and forward scan in control samples was only ∼13.68% with a champion PCE = 14.01% under the forward scan (Table S5, Supporting Information). Figure 1b shows the current density vs voltage (J-V) curve of the champion control and the RP device under reverse and forward scans. Both of the control and RP device had open-circuit voltages (V_{oc}) of ≈1.16 V, and negligible hysteresis as indicated by the low hysteresis index |PCE$_{reverse}$ − PCE$_{forward}$|/PCE$_{reverse}$; i.e., ≈5% for the control devices and ≈3% for the RP devices.[19] However, the RP devices had much higher J_{sc} (19.34 mA cm^{-2}) than the control devices J_{sc} (17.30 mA cm^{-2}). The use of RP achieved a notably high PCE and the highest J_{sc} compared to reported PeNC solar cells that have PCE of >12% and negligible hysteresis (Figure 1c; Table S6, Supporting Information). The external quantum efficiency (EQE) spectra confirmed the J_{sc} (Figure S3, Supporting Information). The integrated J_{sc} from EQE spectra were
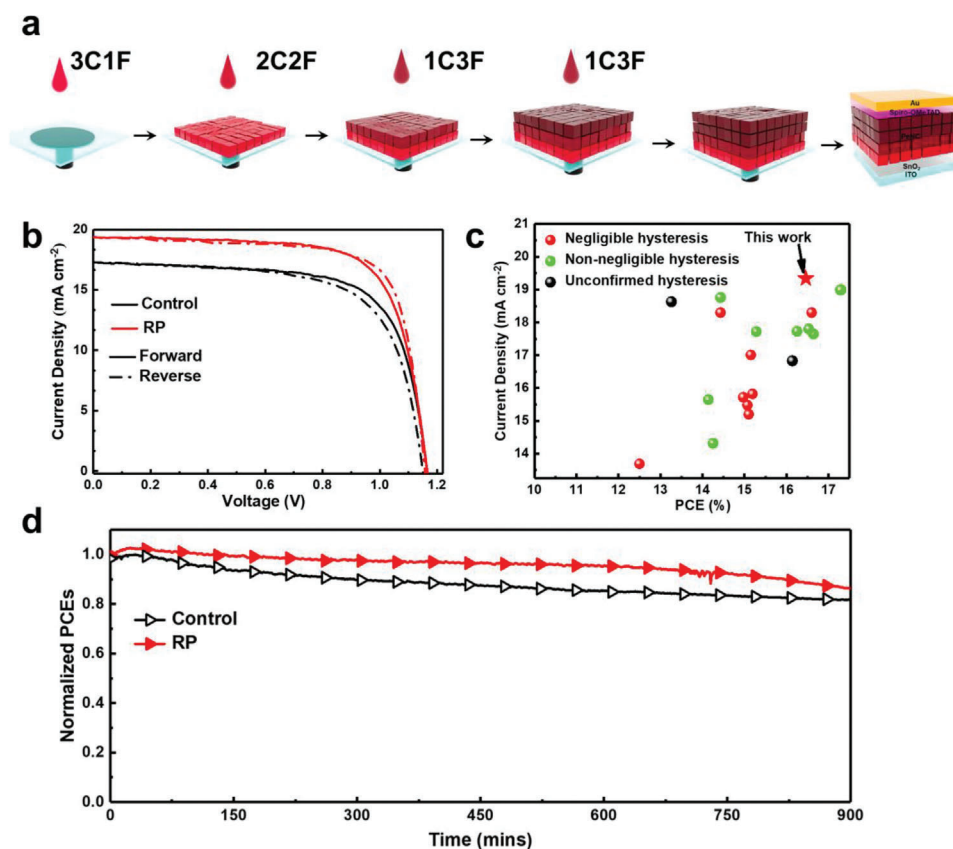
Figure 1. a) Schematic of fabricating gradient-bandgap PeNC films and the device structure. b) *J*–*V* curves of the champion control and RP device. c) Summary of the J_{sc} as a function of PCEs for PeNC solar cells. d) MPP tracking for the encapsulated control and RP device under continuous 1 sun illumination at 21 °C with a relative humidity of <1%.

19.30 mA cm^{-2} for the RP device and 17.29 mA cm^{-2} for the control device, which are consistent with the J_{sc} obtained from the *J*–*V* curve. The EQE spectra also indicated that the increased J_{sc} for RP devices was attributed to the increased carrier-extraction efficiency. The bandgap E_g extracted from the EQE spectra was lower in the RP device ($\approx$1.60 eV) than in the control device ($\approx$1.64 eV). The absorbance spectra and Tauc plot (Figure S4, Supporting Information) indicated that RP caused a redshift in E_g of PeNC films, which was consistent with the EQE spectra. Thus, considering the same V_{oc} of control and RP devices, it was indicated that the V_{oc} loss decreased to 440 meV in the RP device from 480 meV in the control device.

In addition, the RP method gave better reproducibility than the control method (Figure S5, Supporting Information). The average PCE was higher and less variable in the RP devices (15.42 ± 0.46%) than in the control devices (12.11 ± 0.78%). The RP devices had good stability at the maximum power point (MPP) under continuous 1 sun illumination at 21 °C with a relative humidity of <1%. The encapsulated RP devices retained 90% of their initial PCE after 900 min of 1 sun illumination at MPP (Figure 1d), and also showed good storage stability for >600 h in ambient condition (Figure S6, Supporting Information). Interestingly, the PCE of the RP device increased slightly after 200 h, then decreased after 400 h; this trend may be due to a spontaneous passivation phenomenon that can occur in perovskite solar cells

(Figure S6, Supporting Information).[20,21] Above results suggest that the RP method can increase the J_{sc} and reduce the V_{oc} loss, and that these changes lead to increased PCEs accompanied by better stability.

To identify the origin of the increased J_{sc}, we first examined the X-ray diffraction (XRD) pattern and Fourier-transform infrared spectra (FTIR) to compare the crystallite size and residual long-chain ligands in the PeNC films treated by the control method or the RP method, because the charge confinement induced by the small particle size and long-chain ligands is the most critical hindrance for J_{sc}. The (110) peak in the XRD pattern (**Figure 2**a) of the RP sample had higher intensity and a narrower full-width at half-maximum (0.29°) than the control sample (0.51°). More importantly, the crystallite size obtained by the Scherrer equation was increased to 55.28 nm in the RP samples from 30.67 nm in the control samples. This change indicates that RP enhanced the crystallinity and increased crystallite size of PeNC films. Grazing-incidence wide-angle X-ray scattering (GI-WAXS) showed the crystal orientation of PeNC films (Figure S7, Supporting Information). The control films exhibited a strong δ phase at $q \approx 0.7$ Å^{-1} compared to the RP films (left panel of Figure S7, Supporting Information). In addition, the azimuthal-angle plot along the ring at $q \approx 1$ Å^{-1} (right panel of Figure S7, Supporting Information), revealed that the control films showed a random orientation, whereas the RP films presented a
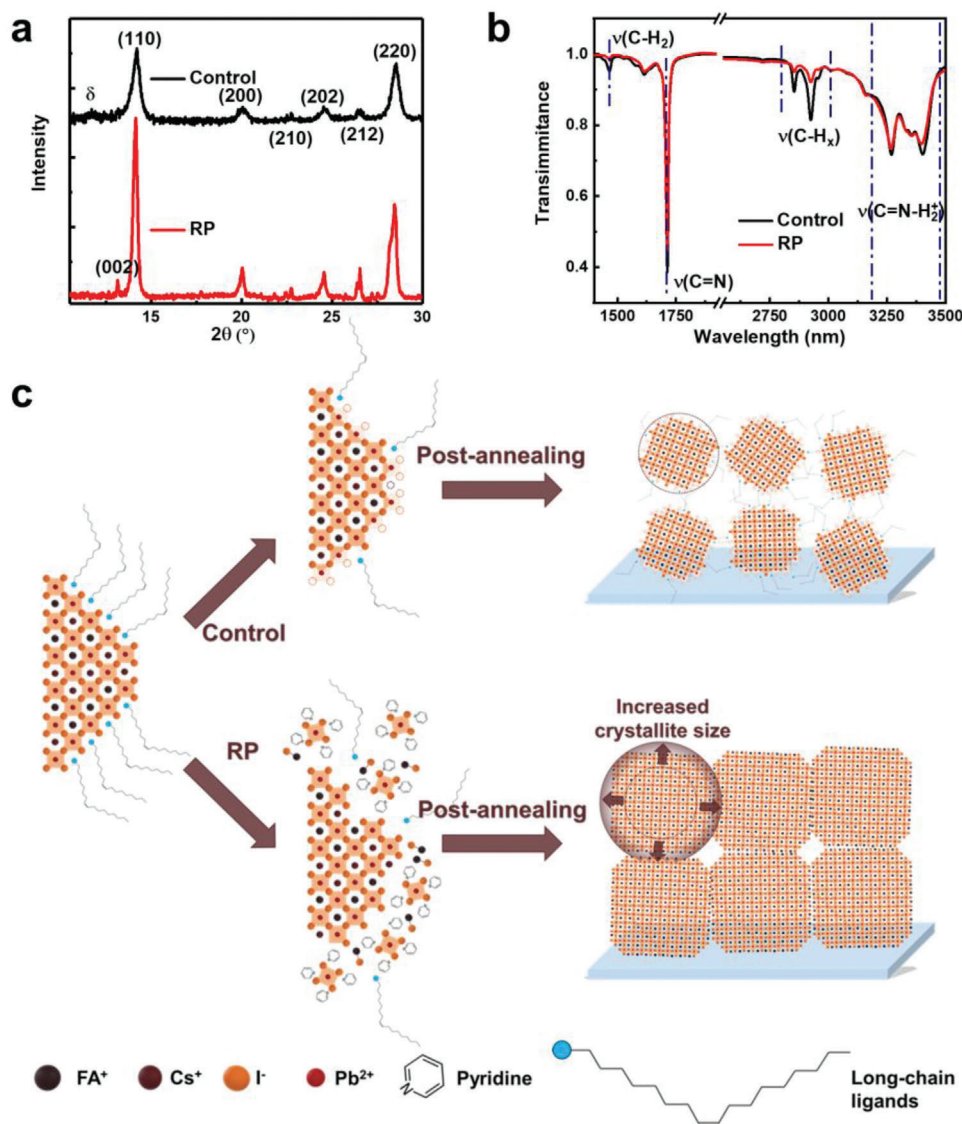
Figure 2. a) XRD and b) FTIR pattern of control and RP films. c) The schematic of the control method and RP method.

pronounced orientation at an azimuth angle of 90°; i.e., the crystal orientation in the RP films were preferentially perpendicular to the substrate. The weak δ phase and more orientated stacking in RP films would be beneficial to the long-term stability and carrier transport of RP samples.[22,23] Then we measured the FTIR of the PeNC films to quantify the presence of residual long-chain ligands in the PeNC films (Figure 2b). The intensity of the alky stretching vibrations (ν(C−H$_x$) = 2800−3000 cm^{-1} and ν(C−H$_x$) = 1464 cm^{-1}) in FTIR of the RP samples was decreased compared to control samples, suggesting that less long-chain ligands remained in the RP sample than in the control sample.

Together, these results demonstrate that RP can increase the crystallite size of PeNC film and more efficiently remove the long-chain ligands in the PeNC films. Previously, many reports about polycrystalline perovskite solar cells have demonstrated that the [PbI$_6$]$^{4-}$ and pyridine can form a complex due to the strong chemical bonding between them, and pyridine vapor can even quench

the polycrystalline perovskite films.[24,25] We found that pyridine could also bleach the colloidal perovskite nanocrystal solution (Figure S8, Supporting Information). This color change is consistent with previous reports, and supported the formation of complex (Figure S8, Supporting Information).[24,25] Considering this result, we suggest a mechanism to explain the origin of the increased crystallite size and removed long-chain ligands by RP (Figure 2c): the chemical bonding between [PbI$_6$]$^{4-}$ and pyridine is stronger than that between the long-chain ligands and the colloidal perovskite nanocrystals, so the pyridine used in the RP method isolates the long-chain ligands from the surface of colloidal perovskite nanocrystals. As a result, the IPA in the RP method can efficiently remove the long-chain ligands, and permit FA$^+$ to replace them. The loss of long-chain ligands strengthens the coaction effect between perovskite nanocrystals, and thereby lead to more orientated PeNC films. Concurrently, FAI in the RP method interacts with the complex of [PbI$_6$]$^{4-}$ and pyridine, so
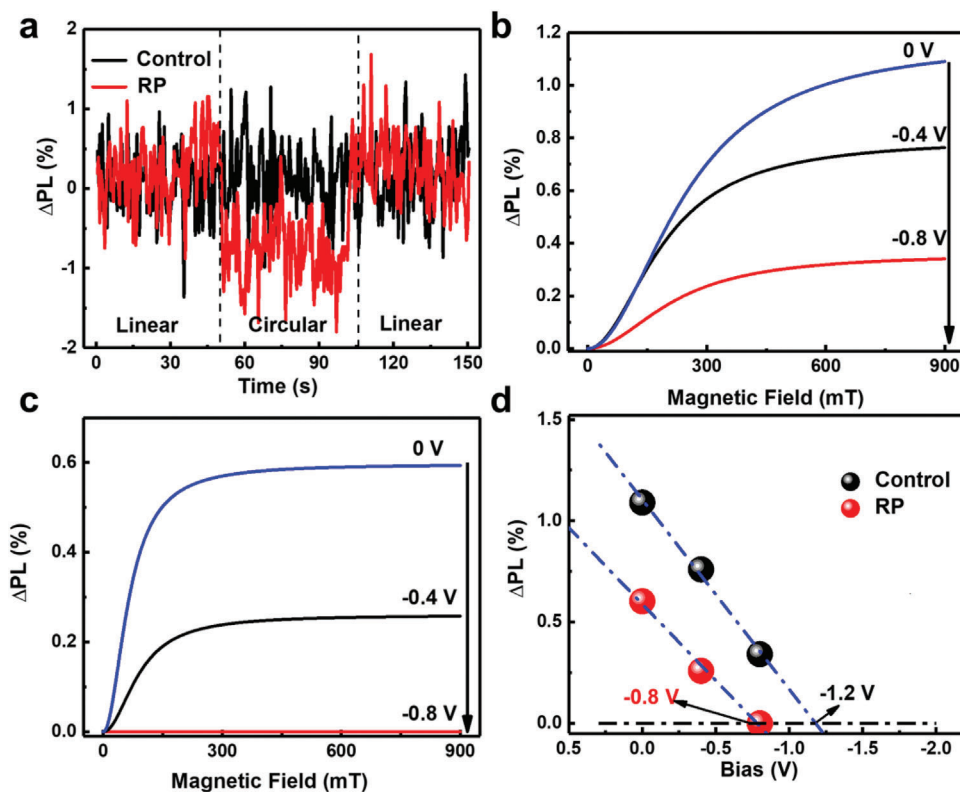
Figure 3. a) PL intensity changed by switching the photoexcitation polarization from linear to circular. b,c) MFE of PL measured at different reverse biases for Control (b) and RP (c) devices. d) Amplitude change of MFE of PL vs reverse biases at 900 mT with an excitation intensity of 343 mW by a 405 nm continuous-wave laser.

the PeNC films re-assemble with larger crystallite size than in control films. In addition, during this process, the concentration of FAI is higher in IPA than in EtOAc, so additional FAI will be inserted into the PeNC films, resulting in the decreased bandgap of PeNC film (Figure S4, Supporting Information).

This proposed mechanism also can explain why the pure IPA with FAI cannot increase the device PCEs, and why excess pyridine decreases the device PCEs (Table S2, Supporting Information). For pure IPA with FAI or insufficient pyridine, the combination between the long-chain ligands and the colloidal perovskite nanocrystals cannot be broken completely, and no complex can form to assist the re-assembly of PeNC films. In contrast, if pyridine content is too high, an overabundance of complex formed, which cannot be fully converted to perovskite phase, so the film degraded. In general, by carefully optimizing the RP method, the crystallite size of PeNC films can be increased while minimizing the number of residual long-chain ligands in the PeNC films.

The increased crystallite size and removal of long-chain ligands should overcome the charge-confinement effect in the PeNC film, and may lead to the reduced E_b and facilitated exciton dissociation. To confirm this conjecture, we investigate the exciton behavior to obtain insight about exciton dissociation in the PeNC films. In photoexcitation-polarization-dependent PL measurements (**Figure 3**a), the RP films generated higher PL intensity under linearly polarized photoexcitation than under circularly polarized photoexcitation; i.e., ΔPL (the change of PL inten-

sity) was negative when the polarization of photoexcitation was switched from linear to circular. In contrast, the control films did not exhibit any detectable ΔPL upon switching between linearly and circularly polarized photoexcitations. This comparison provided two critical insights.[26–28]

The first insight is that photogenerated excitons undergo exciton–exciton interaction in the RP films. If this exciton–exciton interaction is absent, linearly and circularly polarized photoexcitation generated the same quantity of excitons, so the ΔPL phenomenon did not occur.[29] Thus, the negative ΔPL was direct evidence that the RP method can increase the number of excitons that were available to be converted to photocurrent in solar cells. Exploitation of the ΔPL phenomenon to compare exciton densities between samples does not require collecting total PL yield, and is therefore a reliable method to compare exciton densities between samples.

The second insight is that when exciton–exciton interaction occurred, parallel-oriented orbital magnetic dipoles between excitons caused a reduction in the number of light-emitting excitons. This phenomenon was revealed by the lower PL intensity under a circularly polarized photoexcitation as compared to antiparallel-oriented orbital magnetic dipoles under linearly polarized photoexcitation. This provided a deeper understanding that internal magnetic interaction was a major cause of the loss of light-emitting excitons.

Then we checked the temperature-dependent PL spectra of the bare PeNC films to evaluate the E_b (Figure S9,
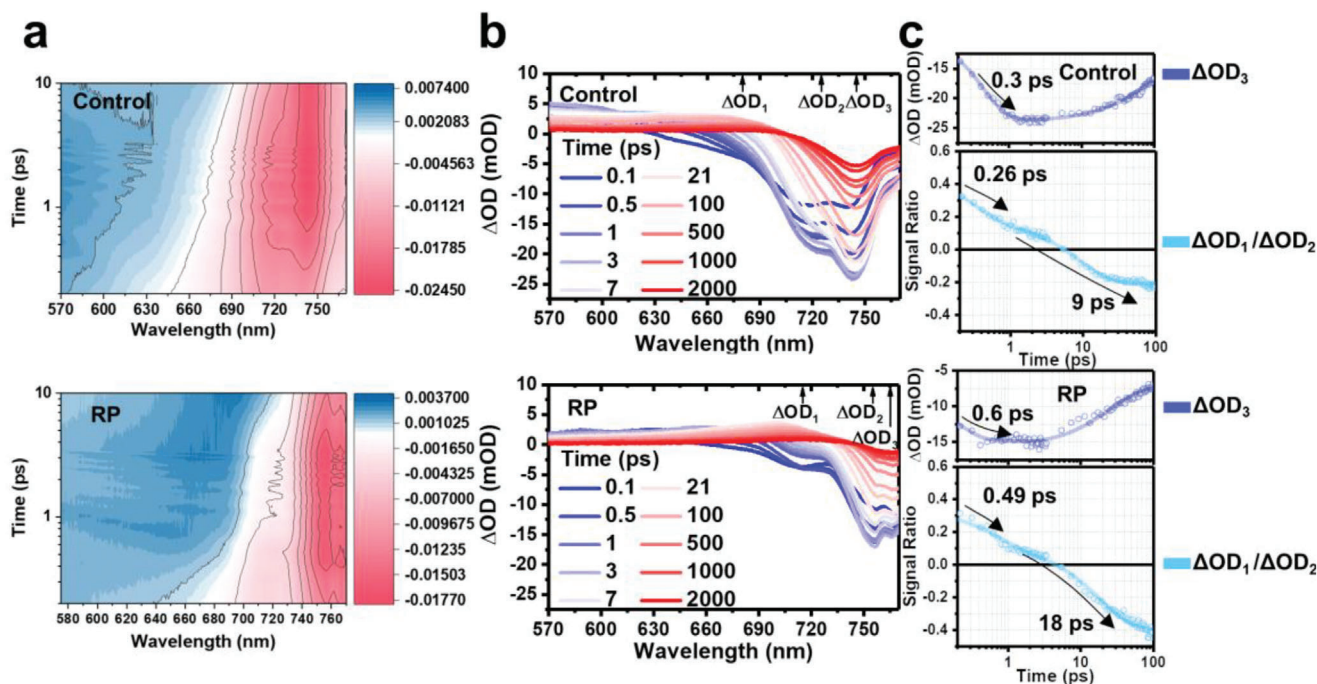
Figure 4. Transient absorption spectra (TAS) of the bare PeNC films. a) Pseudo-color TAS mapping for the initial 10 ps, b) Representative TAS, and c) the signal ratios of $\Delta OD_1/\Delta OD_2$ and the signal of ΔOD_3 as a function of time for the bare control (top panel) and bare RP films (bottom panel).

Supporting Information) by fitting the PL intensity as a function of $(k_B T)^{-1}$, where k_B is the Boltzmann constant and T is the absolute temperature.[30] The E_b of RP films was 31.61 ± 1.78 meV, and that of control films was 36.29 ± 1.76 meV . This result confirms that the RP method decreased E_b in the resulting PeNC films. Temperature dependent PL measurement has the limitations that it can only examine bare PeNC films, and is affected by defects in the PeNC films, so we further exploited the magnetic-field effect (MFE) of PL at different biases to evaluate the E_b under operation condition and to elucidate how E_b affects exciton dissociation in PeNC solar cells. The MFE of PL can be observed when an external magnetic field disturbs the internal conversion between different spin states of the exciton; especially, a magnetic field can completely remove the possibility of involving detrapped carriers upon applying an external bias. Therefore, measuring MFE of PL at different biases provides a unique method to estimate the E_b in PeNC device. (However, simple measurement of bias-dependent PL may not accurately represent E_b, because an external bias can de-trap trapped carriers and indirectly change PL intensity.) In control and RP devices, the PL intensity gradually increased as the magnetic field increased (Figure 3b,c). Applying an external bias can continuously decrease the amplitude of MFE of PL. The critical bias required to completely quench the signal of MFE of PL provides a direct in situ method to estimate E_b.[31,32] The control devices required -1.2 V to completely quench the signal of MFE of PL, whereas the RP devices just required -0.8 V to completely quench the signal of MFE of PL (Figure 3d). We also validated this at a different excitation intensity and obtained consistent results that the critical bias required to quench the MFE of PL was decreased in RP samples (Figure S10, Supporting Information). The lower magnitude of

critical bias for RP devices than for control devices demonstrated that excitons in the RP samples are much easier to dissociate because of the decreased E_b. In conclusion, RP treatment weakened charge confinement, and thereby reduced E_b and facilitated exciton dissociation in PeNC films.

Furthermore, overcoming the charge confinement by removing long-chain ligand in the PeNC films may facilitates carrier transport in the PeNC solar cells. This means that the reduction in the number of long-chain ligands in the RP film compared to the control film may result in smoother carrier transport and extraction in the RP sample than in the control sample.

To confirm this, we conducted transient absorption spectroscopy (TAS) for bare PeNC films (**Figure 4**a). Bare control and bare RP films showed broad photobleaching ($\Delta OD < 0$) in the spectral range from 680 nm to 770 nm (Figure 4b), and the broad photobleaching region also demonstrates the formation of gradient-bandgap structure in the PeNC film that is composed of three different bandgap perovskite nanocrystals. In addition, the overall photobleaching region of the RP sample was redshifted compared to the control sample, which is consistent with the absorbance spectra.

Within the broad photobleaching region, we examined three specific wavelength signals (Control films: 680 nm, 725 nm, 745 nm; RP films: 715 nm, 755 nm, 765 nm) and refer them as ΔOD_1, ΔOD_2, and ΔOD_3 which correspond to the high-energy-level excited state, intermediate-energy-level excited state and low-energy-level excited state respectively, to track the hot-carrier cooling process.[33–35] The hot carriers cool from the high-energy-level excited state (ΔOD_1), to the intermediate-energy-level excited state (ΔOD_2), then to the low-energy-level excited state (ΔOD_3). Thus, we evaluated the

ADVANCED
SCIENCE NEWS
www.advancedsciencenews.com

ADVANCED
MATERIALS
www.advmat.de
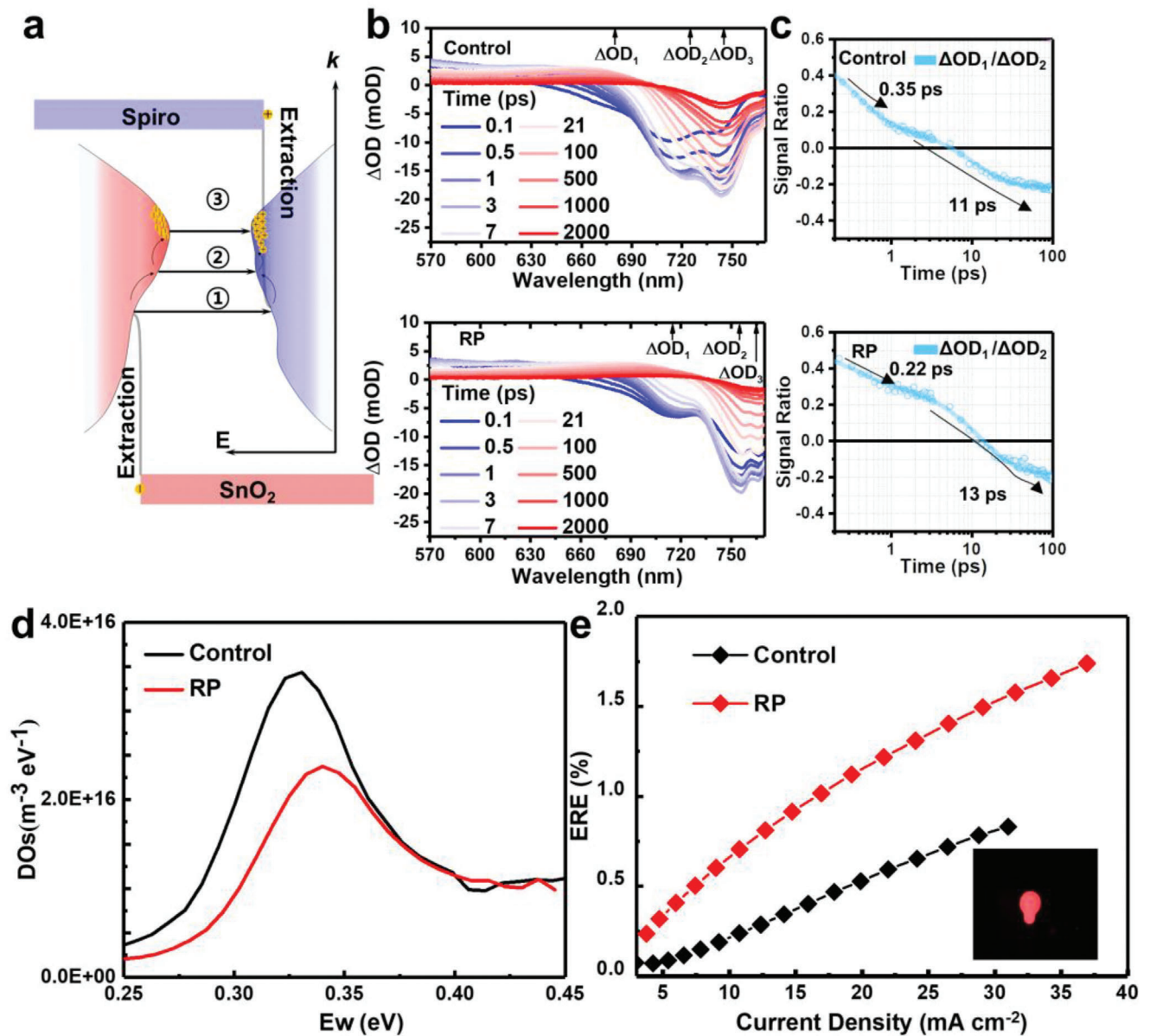
Figure 5. a) Simple energy diagram for gradient-bandgap PeNC solar cells. b) Representative TAS, and c) the signal ratios of $\Delta OD_1/\Delta OD_2$ as a function of time for the control (top) and RP films (bottom) sandwiched by transporting layers. d) tDOS of control and RP devices. e) ERE vs current density in darkness (inset is the lighting image of RP devices).

hot-carrier cooling process by tracking the signal ratios of $\Delta OD_1/\Delta OD_2$ and the signal of ΔOD_3 (Figure 4c), and the decay profiles were fitted by bi-exponential function. Hot carriers cool on a femtosecond scale,[33] so we choose fast decay stage of the $\Delta OD_1/\Delta OD_2$ to evaluate the hot-carrier cooling process. In the RP films, the signal ratio of $\Delta OD_1/\Delta OD_2$ showed a decay time constant = 0.49 ps. In contrast, in the control films, the signal ratio of $\Delta OD_1/\Delta OD_2$ diminished quickly with a decay constant = 0.26 ps, indicative of fast hot-carrier cooling process. The signal of ΔOD_3 first decayed at early stage due to the cooled carriers that descended from the high-energy state, and then increased due to the carrier-recombination process. ΔOD_3 of RP films at the early stage had a decay constant = 0.6 ps, whereas control films had a

shorter decay constant = 0.3 ps. These results demonstrate that the hot-carrier cooling process was decelerated in the RP samples.

A simple energy diagram of the gradient-bandgap PeNC film with transporting layer was shown in **Figure 5**a. The formed free carriers would relax along the energy band tail from the high-energy state to the low-energy state, and then be extracted by corresponding transporting layers at the interface. We checked the carrier-extraction condition by conducting TAS on PeNC films sandwiched by the electron-transporting layer (ETL) and hole-transporting layer (HTL) (Figure 5b; Figure S11, Supporting Information). When the PeNC films are sandwiched by the ETL and HTL, the signal ratio of $\Delta OD_1/\Delta OD_2$ is related to charge

**ADVANCED
SCIENCE NEWS**

www.advancedsciencenews.com

**ADVANCED
MATERIALS**

www.advmat.de

extraction from the PeNC films to the ETL and to the carrier-relaxation process. To track the hot-carrier behavior, we plotted the decay profiles of $\Delta OD_1/\Delta OD_2$ (Figure 5c). In the RP films with ETL, the decay rate of the $\Delta OD_1/\Delta OD_2$ was accelerated (decay constant = 0.22 ps, Figure 5c) compared to the bare RP films (decay constant 0.49 ps, Figure 4c). In contrast, in the control films with the ETL, the decay rate of $\Delta OD_1/\Delta OD_2$ was decelerated (decay constant = 0.35 ps, Figure 5c) compared to the bare control film (decay constant = 0.26 ps, Figure 4c). These differences indicate that the carrier extraction between the PeNC films and ETL is smoother in the RP devices than in the control devices.

To compare the extraction of ground-state carriers at the interface of PeNC films and transporting layers, we conducted the time-resolved PL (TRPL) measurement (Figure S12, Supporting Information). The TRPL results were fitted by a bi-exponential decay function; in this case, the short lifetime corresponds to quenching via traps or charge transfer, and the long lifetime corresponds to radiative carrier recombination.[36–37] The fitted result and average carrier lifetime (τ_{ave}) were obtained (Table S7, Supporting Information). The bare RP films had $\tau_{ave} = 9.95$ ns, whereas bare control film had $\tau_{ave} = 1.09$ ns; the increased τ_{ave} indicates reduced defects in the bare RP film. Application of HTL and ETL decreased τ_{ave} in both films, but to differing degrees. In the RP film, application of HTL decreased τ_{ave} by 89% to 1.13 ns and application of ETL decreased it by 86% to 1.35 ns. In contrast, in the control film, application of HTL decreased τ_{ave} by 56% to 0.48 nm and application of ETL decreased it by 54% to 0.50 ns. The more pronounced decrease of PL lifetime in the RP device than in the control device demonstrates that charge extraction is more efficient in the RP devices than in the control devices.

This smoother carrier extraction was also confirmed by impedance spectra (Figure S13, Supporting Information). The Nyquist plots showed two semicircles at different frequencies; an equivalent circuit (inset of Figure S13, Supporting Information) was developed to fit this result (Table S8, Supporting Information).[38] In addition, the time constants τ for the bulk (τ_{bulk}) and surface ($\tau_{surface}$) can be obtained according to the resistor–capacitor (RC) circuit model. Here, we assign the longer of the two time constants to bulk recombination, because the bulk of films usually has fewer defects than the surface.[39] The resistance R_{bulk} of RP device was 132.9 ± 10.13 Ω which was much lower than that of the control devices ($R_{bulk} = 236.5 \pm 13.34$ Ω). This difference demonstrated the improved charge transport in the RP samples. In addition, both τ_{bulk} and $\tau_{surface}$ were longer in the RP sample than in the control sample. This comparison demonstrates that defect-assisted recombination was lower in the RP samples than in the control samples.

These results confirm that use of the RP to overcome the charge confinement in the PeNC film, also increased the carrier transport and extractions in the PeNC solar cells. In addition, we can conclude that by overcoming the charge confinement in the PeNC film, both the exciton dissociation and carrier extraction were improved; as a result, J_{sc} increased.

The decreased V_{oc} loss in the RP devices compared to the control devices should be due to the reduced defect density compared to the control devices. To confirm this supposition, we used thermal-admittance spectroscopy analysis to quantize the defect density in the PeNC films. The trap density of states (tDOS) can

be derived from the angular-frequency-dependent capacitance as[40,41]

$$N_T\left(E_\omega\right) = -\frac{V_{bi}dC\omega}{qWd\omega k_B T} \tag{1}$$

where q is the elementary charge, V_{bi} is the built-in potential and W is the depletion width, which can both be obtained using Mott–Schottky analysis (Figure S14a,b, Supporting Information), C is the measured capacitance, and ω is the applied angular frequency. The RP devices had a $V_{bi} = 1.07$ V, and the control devices had a $V_{bi} = 1.06$ V. The demarcation energy E_ω is defined as

$$E_\omega = k_B T \cdot \ln\left(\frac{\omega_0}{\omega}\right) \tag{2}$$

where ω_0 is the attempt-to-escape angular frequency, which can be extracted from the temperature-dependent capacitance (Figure S14c–f, Supporting Information). The obtained tDOS was lower in the RP devices than in the control devices in an energy depth range of 0.25 eV to 0.35 eV (Figure 5d).

We also measured the light intensity dependent V_{oc} to quantify the trap-assisted carrier recombination (Figure S15, Supporting Information). The ideality factor of RP device ($n = 1.44$) obtained from light intensity-V_{oc} relationship was lower than that of the control device ($n = 1.73$); the difference indicates that trap-assisted non-radiative recombination was lower in the RP device than in the control device.[42] These results demonstrate that RP can passivate defects more effectively than the conventional method; this difference accounts for the reduced V_{oc} loss and decelerated hot carrier cooling in RP samples, compared to control samples.[43,44]

The external radiation efficiency (ERE_{EL}) of solar cells as light-emitting diodes with charge injection in darkness is a valid parameter to evaluate the V_{oc} loss induced by non-radiative recombination ($\Delta V_{non-rad,loss}$) as[45,46]

$$\Delta V_{non-rad,loss} = -k_B T \cdot \ln\left(ERE_{EL}\right) \tag{3}$$

Thus, the higher ERE_{EL} means lower non-radiative recombination losses. To confirm the $\Delta V_{non-rad,loss}$, we measured the ERE_{EL} of the solar cells in darkness (Figure 5e). The RP device had an $ERE_{EL} = 1.12\%$ at current density = 19.30 mA cm^{-2}, and the device showed bright electro-luminance (inset of Figure 5e). As expected, ERE_{EL} was higher in the RP devices than in the control devices; this difference was consistent with the reduced V_{oc} losses in the RP devices. Thus, we concluded that the RP could build more robust passivation than the conventional treatment method, and thereby reduce V_{oc} losses that result from defect-assisted non-radiative recombination.

3. Conclusions

We demonstrated a simple RP for PeNC films to overcome charge confinement, by utilizing a mixture of IPA and pyridine. The strong chemical bonding between $[PbI_6]^{4-}$ and pyridine allows pyridine to isolate the long-chain ligand from the surface of colloidal perovskite nanocrystals, and thereby facilitates removal of the long-chain ligands by IPA. Subsequently, the interaction of

**ADVANCED
SCIENCE NEWS**

www.advancedsciencenews.com

**ADVANCED
MATERIALS**

www.advmat.de

FAI with the complex of pyridine and $[PbI_6]^{4-}$ promotes the re-assembling process, and thus increases the crystallite size of PeNC films. As a consequence of the removal of long-chain ligands and increase in crystallite sizes, the charge confinement in the PeNC film was overcome; this change facilitated exciton dissociation and improved carrier extraction in PeNC solar cells. Additionally, due to the good solubility of FAI in pyridine/IPA, this strategy can provide robust passivation for the PeNC solar cells, which suppresses the non-radiative recombination loss in them. As a result, a high current density of 19.30 mA cm^{-2} and a PCE of 16.46% were obtained by the RP method due to the increased J_{sc} and reduced V_{oc} loss. This work provides a new direction to further increase the PCEs of PeNC solar cells. We believe that this RP method for post-treatment and re-assembling is also applicable to other perovskite films, including polycrystalline and single-crystal perovskites, pointing out a new insight to engineer perovskite optoelectronic devices.

4. Experimental Section

Materials: Cesium carbonate (Cs$_2$CO$_3$, 99.9%), oleylamine (OLA, technical grade 70%), oleic acid (OA, technical grade 90%), octane (anhydrous, $\geq$ 99%), methyl acetate (MeOAc, anhydrous 99.5%) and ethyl acetate (EtOAc, anhydrous 99.5%), toluene (anhydrous 99.8%), chlorobenzene (anhydrous, 99.8%), 4-tert-butylpyridine (96%, Aldrich), lead(ii) nitrate (Pb(NO$_3$)$_2$, 99.999%), formamidine acetic acid salt ($\geq$ 99%), potassium thiocyanate (KSCN, 99.0%), bis(trifluoromethane)sulfonimide lithium salt (Li-TFSI), and acetonitrile (anhydrous, 99.8%) were purchased from Sigma Aldrich. 1-Octadecene (ODE, technical grade 90%) and SnO$_2$ nanoparticle dispersion (15% in H$_2$O) were purchased from Alfa Aesar. Lead(II) iodide (PbI$_2$ 99.9985%) was purchased from Tokyo Chemical Industry (TCI). (2,2',7,7'-tetrakis(N,N-di-p-methoxyphenylamine)−9,9-spirobifluorene (spiro-OMeTAD, $\geq$99.5%) was purchased from Luminescence Technology corporation (Lumtec). Hexane (reagent grade $\geq$95%) was purchased from Samchun Chemicals. All chemicals were used without further purification.

Synthesis of Colloidal Perovskite Nanocrystals: CsPbI$_3$ colloidal nanocrystals were synthesized following a previous report[47] with some modifications. Cs-oleate precursor was obtained by dissolving 0.12 g Cs$_2$CO$_3$ in 0.48 mL OA and 12 mL ODE, then the mixture was loaded into a 100 mL three-necked flask and stirred under vacuum for 1 h at 120 °C. Lead precursor was obtained by dissolving 1.2 g PbI$_2$ in 60 mL ODE, 6 mL OA, and 6 mL OLA, then the mixture was loaded into a 250 mL flask and stirred under vacuum at 120 °C for 1 h. The flasks were then filled with N$_2$ and kept under constant N$_2$ flow. The temperature of lead precursor was increased to 160 °C, then 9.6 mL of the Cs-oleate precursor was swiftly injected into the mixture; 5 to 10 s later, the reaction was quenched by immersing the flask in an ice bath. After it had cooled to room temperature, the solution was separated into six centrifuge tubes with 12 mL solution in each. Then 30 mL of anhydrous MeOAc was added to each tube, and the mixture was centrifuged at 8000 rpm for 5 min. The supernatant was discarded, then the remaining nanocrystal precipitate was dispersed by adding 4 mL toluene to each tube; therefore a total of 24 mL CsPbI$_3$ colloidal nanocrystal solution was obtained.

FAPbI$_3$ colloidal nanocrystals were synthesized as follows. FA-acetate (0.6515 g), ODE (20 mL), and OA (10 mL) were added to a 100 mL three-neck flask and dried under vacuum for 20 min at room temperature. Then the mixture was then heated to 80 °C under N$_2$ atmosphere for 1 h. PbI$_2$ (1.044 g), ODE (60 mL), OA (12 mL), and OLA 6 mL) were stirred in a 250 mL flask and stirred under vacuum at 120°C for 1 h; then the temperature of the flask was decreased to 80 °C under N$_2$ atmosphere, then FA-oleate precursor (24 mL) was injected into the Pb-Flask, and 15 s later, the mixture was quenched in an ice-water bath. After the solution had cooled to room temperature, it was separated to three tubes with 32 mL solution

in each tube. Then MeOAc (8 mL) was added to each tube, and the mixture was centrifuged at 7500 rpm for 10 min. The supernatant was discarded, then the resulting nanocrystal precipitate was dispersed by adding 8 mL toluene to each tube, to yield a total of 24 mL FAPbI$_3$ colloidal nanocrystal solution.

Then CsPbI$_3$ nanocrystal solution and FAPbI$_3$ nanocrystal solution were mixed at volume ratios of 3:1, 2:2, and 1:3 and kept rotating for 1 h to obtain 3C1F nanocrystals, 2C2F nanocrystals, and 1C3F nanocrystals, respectively. The resultant mixed-cation colloidal nanocrystals were purified by adding EtOAc (volume ratio of colloidal nanocrystal solution to EtOAc was 1:2) and centrifuged at 8000 rpm for 5 min. The supernatant was discarded, then the obtained nanocrystals were dispersed in 15 mL hexane and stored in a refrigerator at 7 °C overnight. Then the colloidal nanocrystal solutions were centrifuged at 4000 rpm for 5 min to remove the precipitate and dry the supernatant under vacuum. Finally, the nanocrystals were dispersed in octane to a concentration of 80 mg mL^{-1} for each composition.

Device Fabrication: Saturated Pb(NO$_3$)$_2$ in MeOAc solution and FAI in EtOAc solution were prepared as reported previously.[47] For the optimal RP method, 5 mg mL^{-1} FAI was dissolved in IPA, and the solution was mixed with pyridine at a volume ratio of 100:5 (IPA:Pyridine) to obtain RP solution. The spiro-OMeTAD solution was prepared by dissolving 72.3 mg of spiro-OMeTAD in 1 mL of chlorobenzene, then adding 28.8 μL of 4-tert-butylpyridine and 17.5 μL of Li-TFSI (520 mg mL^{-1} in acetonitrile) solution. Glass/ITO substrates were cleaned sequentially in acetone and IPA by sonication for 15 min each, then boiled in IPA on a hot plate at 300°C to evaporate the solvent quickly from the substrates. The cleaned substrates were further treated in an ultraviolet–ozone chamber for 20 min before use. Then 15 wt% SnO$_2$ (Alfa Aesar) nanoparticle solution was diluted using KSCN solution (2 mg mL^{-1} in deionized water) to 3 wt% and spin-coated onto glass/ITO substrates at 3000 rpm for 30 s, then baked on a hot plate in air at 150 °C for 30 min.

To obtain gradient-bandgap PeNC films, the 3C1F nanocrystals ($\approx$80 mg mL^{-1} in octane) were spin-coated on SnO$_2$ substrate at 2,000 rpm for 30 s first, then the 2C2F nanocrystals ($\approx$80 mg mL^{-1} in octane) were spin-coated on top of the 3C1F nanocrystal layer at 2000 rpm for 30 s, then the 1C3F nanocrystals ($\approx$80 mg mL^{-1} in octane) were spin-coated twice on top of these two layers, at 2000 rpm for 30 s. After each spin-coating of nanocrystals, the films were washed twice using saturated Pb(NO$_3$)$_2$ solution, then rinsed once using pure anhydrous MeOAc; the resulting PeNC films had a thickness of $\approx$320 nm. The RP samples were treated using RP solution by spin-coating at 3000 rpm for 30 s, then annealed on a hot plate at 120 °C for 10 min in air. The control samples were treated using EtOAc with saturated FAI by spin-coating at 3000 rpm for 30 s, then rinsed using MeOAc, then annealed on a hot plate at 120 °C for 10 min in air. All of the above processes were conducted in ambient with a relative humidity of $\approx$20–25%. Finally, the spiro-OMeTAD solution was spin-coated onto the PeNC films at 3000 rpm for 30 s in an N$_2$-filled glove box. The Au electrode was then deposited by thermal evaporation to a thickness of 80 nm. Then, the devices were encapsulated in ambient condition with relative humidity of <10% by using a glass lid and UV-curable epoxy resin with 20 min of UV (365 nm) treatment.

Characterization of Films and Devices: The J–V curves for PCE estimation were measured under AM 1.5G illumination (100 mW cm^{-2}) by a potentiostat (CHI 608C, CH Instruments) with a metal aperture mask that had opening of size 0.05 cm^2. The scan rates of J–V were 120 mV s^{-1}. The AM 1.5G illumination was provided by a solar simulator (PEC-L11, Peccell Technologies) which was calibrated by a standard Si cell (Reference cell: 91150V, Newport, certified date: February 2017) with a quartz filter. The external quantum efficiency (EQE) spectra were collected using a quantum-efficiency measurement system (QUANTX-300, Oriel) in darkness with no electrical bias. The luminance characteristics of the PeNC solar cells were measured using a Minolta CS 2000 spectroradiometer combined with a Precision Source-Measure Unit (Keithley 236). The impedance spectra and Mott–Schottky measurement were performed using an electrochemical workstation (SP-200 potentiostat, Biologic). Thermal admittance spectra were measured by combining the electrochemical workstation with a thermostat (LT-350, CHINO). For MPP tracking, the evolution of

normalized PCEs of the encapsulated PeNC solar cells at maximum power point was measured under 1 sun illumination at 21 °C with a relative humidity of <1%. Transmission electron microscopy images of colloidal perovskite nanocrystals were collected using a JEOL-JEM 2100F microscope. The ultraviolet photoelectron spectroscopy (UPS, AXIS Ultra DLD, Kratos Inc.) utilized a helium-gas discharge lamp with an excitation energy of 21.2 eV and an energy resolution of 200 meV over a diameter of 100 μm sampling area. To mitigate static charge accumulation, a sample bias of 15 V was applied during the measurements.

Photoexcitation-Polarization-Dependent Photoluminescence and Magnetic Field Effects of Photoluminescence: Both the photoexcitation-polarization-dependent PL and the magnetic field effects of PL measurements were obtained using a FLAME-T-XR1-ES spectrometer, and both were excited by a CW laser beam of 405 nm. For the photoexcitation-polarization-dependent, PL was measured upon switching the photoexcitation between linear and circular polarizations at the same intensity by rotating a quarter wave plate with 0° and 45° relative to a linear polarizer. The magneto-photocurrent measurements were performed under an external magnetic field (*B*) parallel to the device plane scanning from 0 to 900 mT.

Femtosecond Transient Absorption Spectroscopy: The femtosecond transient absorption (fs-TA) spectroscopy was set up as described elsewhere.[48,49] The fs-TA measurements were conducted using a home-built pump–probe system. A Ti:sapphire laser system (Spectra-Physics, Spitfire, 800 nm, 400 μJ, 30 fs) with 10-kHz repetition rate was applied as the fundamental laser source of the fs-TA spectrometer. The output beam was divided by a beam splitter with an equivalent ratio. A pulse of 200 μJ was used to pump a commercial optical parametric amplifier (TOPAS, Light Conversion) and a pump pulse of 490 nm was generated; its polarization was set at the magic angle (54.7°) to the vertically-polarized probe by using a half-wave plate (Thorlabs) and a Glan-laser polarizer (Thorlabs). The rest of the fundamental light was used to generate the probe pulse; white light continuum (WLC) probe pulses were generated by focusing a small portion of the transmitted fundamental 800-nm pulses onto using a CaF$_2$ window (3 mm thick). The excited spot was probed using white-light-continuum probe pulses. The time delay between pump and probe beams was carefully controlled by making the pump beam travel along a variable optical delay (ILS250, Newport). The transient absorption difference signal (Δ*A*) at a specific time was obtained by using an optical chopper (MC1F10, Thorlabs) to chop the pump pulses at 500 Hz. Cross-correlation full-width at half-maximum in the fs-TA experiments was ≈200–300 fs. For fs-TA measurements, a quartz cell of that had 2 mm path length (21/Q/2, Starna) was used to minimize chirp.

Photoluminescence Spectra and Time-Resolved Photoluminescence Spectra: PL spectra for colloidal perovskite nanocrystal solution were recorded using a JASCO FP8500 spectrofluorometer. Temperature-dependent PL was measured using a FluoTime 300 spectrometer combined with a closed-cycle helium cryostat CS-204. A picosecond-pulse laser head (LDH-P-C-405B, PicoQuant) was used to excite the samples at a laser wavelength of 405 nm. Time-resolved PL was measured using a FluoTime 300 spectrometer combined with a photon-counting detector (PMA Hybrid 07) and time-correlated single-photon-counting module (PicoHarp, PicoQuant).

Grazing-Incidence Wide-Angle X-ray Scattering: GIWAXS was performed with a wavelength of 0.80771 Å at beamline 3C of the Pohang Accelerator Laboratory (PAL), Republic of Korea. The incident angle on a sample was fixed at 0.3°, and Eiger4M was used to detect the scattered X-ray beam. PLS-II 3C SAXS beamline data plot program with MATLAB (0.1 ver.), and was analyzed by Zenodo.[50]

Supporting Information

Supporting Information is available from the Wiley Online Library or from the author.

Conflict of Interest

The authors have no competing interests.

Data Availability Statement

The data that support the findings of this study are available from the corresponding author upon reasonable request.

[1] T.-W. Lee, I. Sanghyuk, C. Himchan, Y.-H. Kim, US10276807B2, 2019: KR101724210B1, **2015**.

[2] T.-W. Lee, I. Sanghyuk, C. Himchan, Y. Kim, US10263207B2, 2019: KR10186688B1, **2015**.

[3] Y.-H. Kim, S. Kim, A. Kakekhani, J. Park, J. Park, Y.-H. Lee, H. Xu, S. Nagane, R. B. Wexler, D.-H. Kim, S. H. Jo, L. Martínez-Sarti, P. Tan, A. Sadhanala, G.-S. Park, Y.-W. Kim, B. Hu, H. J. Bolink, S. Yoo, R. H. Friend, A. M. Rappe, T.-W. Lee, *Nat. Photonics* **2021**, *15*, 148.

[4] T.-W. Lee, I. Sanghyuk, Y.-H. Kim, C. Himchan, US10193088B2, 2019: KR101703451B1, **2015**.

[5] Y.-H. Kim, J. Park, S. Kim, J. S. Kim, H. Xu, S.-H. Jeong, B. Hu, T.-W. Lee, *Nat. Nanotechnol.* **2022**, *17*, 590.

[6] Y. Liu, H. Wu, G. Shi, Y. Li, Y. Gao, S. Fang, H. Tang, W. Chen, T. Ma, I. Khan, K. Wang, C. Wang, X. Li, Q. Shen, Z. Liu, W. Ma, *Adv. Mater.* **2023**, *35*, 2207293.

[7] M. Hao, Y. Bai, S. Zeiske, L. Ren, J. Liu, Y. Yuan, N. Zarrabi, N. Cheng, M. Ghasemi, P. Chen, M. Lyu, D. He, J.-H. Yun, Y. Du, Y. Wang, S. Ding, A. Armin, P. Meredith, G. Liu, H.-M. Cheng, L. Wang, *Nat. Energy* **2020**, *5*, 79.

[8] D. Jia, J. Chen, R. Zhuang, Y. Hua, X. Zhang, *Adv. Mater.* **2023**, 2212160.

[9] Y.-H. Kim, C. Wolf, H. Kim, T.-W. Lee, *Nano Energy* **2018**, *52*, 329.

[10] H. Min, D. Y. Lee, J. Kim, G. Kim, K. S. Lee, J. Kim, M. J. Paik, Y. K. Kim, K. S. Kim, M. G. Kim, T. J. Shin, S. I. Seok, *Nature* **2021**, *598*, 444.

[11] M. V. Kovalenko, L. Protesescu, M. I. Bodnarchuk, *Science* **2017**, *358*, 745.

[12] L. Liu, A. Najar, K. Wang, M. Du, S. Liu, *Adv. Sci.* **2022**, *9*, 2104577.

[13] A. Miyata, A. Mitioglu, P. Plochocka, O. Portugall, J. T.-W. Wang, S. D. Stranks, H. J. Snaith, R. J. Nicholas, *Nat. Phys.* **2015**, *11*, 582.

[14] L. M. Wheeler, E. M. Sanehira, A. R. Marshall, P. Schulz, M. Suri, N. C. Anderson, J. A. Christians, D. Nordlund, D. Sokaras, T. Kroll, S. P. Harvey, J. J. Berry, L. Y. Lin, J. M. Luther, *J. Am. Chem. Soc.* **2018**, *140*, 10504.

[15] D. Jia, J. Chen, J. Qiu, H. Ma, M. Yu, J. Liu, X. Zhang, *Joule* **2022**, *6*, 1632.

**ADVANCED
SCIENCE NEWS**

www.advancedsciencenews.com

**ADVANCED
MATERIALS**

www.advmat.de

[16] N. Li, S. Tao, Y. Chen, X. Niu, C. K. Onwudinanti, C. Hu, Z. Qiu, Z. Xu, G. Zheng, L. Wang, Y. Zhang, L. Li, H. Liu, Y. Lun, J. Hong, X. Wang, Y. Liu, H. Xie, Y. Gao, Y. Bai, S. Yang, G. Brocks, Q. Chen, H. Zhou, *Nat. Energy* **2019**, *4*, 408.

[17] Q. Zhao, A. Hazarika, X. Chen, S. P. Harvey, B. W. Larson, G. R. Teeter, J. Liu, T. Song, C. Xiao, L. Shaw, M. Zhang, G. Li, M. C. Beard, J. M. Luther, *Nat. Commun.* **2019**, *10*, 2842.

[18] M. Umehara, S. Tajima, Y. Aoki, Y. Takeda, T. Motohiro, *Appl. Phys. Express* **2016**, *9*, 072301.

[19] S. N. Habisreutinger, N. K. Noel, H. J. Snaith, *ACS Energy Lett.* **2018**, *3*, 2472.

[20] E. Jokar, C.-H. Chien, A. Fathi, M. Rameez, Y.-H. Chang, E. W.-G. Diau, *Energy Environ. Sci.* **2018**, *11*, 2353.

[21] Y. Cho, H. D. Kim, J. Zheng, J. Bing, Y. Li, M. Zhang, M. A. Green, A. Wakamiya, S. Huang, H. Ohkita, A. W. Y. Ho-Baillie, *ACS Energy Lett.* **2021**, *6*, 925.

[22] B. Jeong, H. Han, Y. J. Choi, S. H. Cho, E. H. Kim, S. W. Lee, J. S. Kim, C. Park, D. Kim, C. Park, *Adv. Funct. Mater.* **2018**, *28*, 1706401.

[23] J. Chen, D. Jia, R. Zhuang, Y. Hua, X. Zhang, *Adv. Mater.* **2022**, *34*, 2204259.

[24] S. M. Jain, Z. Qiu, L. Häggman, M. Mirmohades, M. B. Johansson, T. Edvinsson, G. Boschloo, *Energy Environ. Sci.* **2016**, *9*, 3770.

[25] H. Zhang, J. Cheng, D. Li, F. Lin, J. Mao, C. Liang, A. K. Y. Jen, M. Grätzel, W. C. Choy, *Adv. Mater.* **2017**, *29*, 1604695.

[26] J. Zhang, B. Hu, *Nano Energy* **2020**, *76*, 104999.

[27] H. Xu, P. Prabhakaran, S. Choi, M. Wang, K.-S. Lee, B. Hu, *J. Phys. Chem. Lett.* **2019**, *11*, 1.

[28] X. Zhu, H. Xu, Y. Liu, J. Zhang, M. Wang, I. N. Ivanov, O. S. Ovchinnikova, B. Hu, *Adv. Mater.* **2019**, *31*, 1901240.

[29] H. Xu, P. Prabhakaran, S. Choi, M. Wang, K.-S. Lee, B. Hu, *J. Phys. Chem. Lett.* **2020**, *11*, 1.

[30] N. Zhou, B. Huang, M. Sun, Y. Zhang, L. Li, Y. Lun, X. Wang, J. Hong, Q. Chen, H. Zhou, *Adv. Energy Mater.* **2020**, *10*, 1901566.

[31] X. Zhu, G. Zhang, J. Zhang, H.-L. Yip, B. Hu, *Joule* **2020**, *4*, 2443.

[32] M. Ahmadi, Y. C. Hsiao, T. Wu, Q. Liu, W. Qin, B. Hu, *Adv. Energy Mater.* **2017**, *7*, 1601575.

[33] M. Li, J. Fu, Q. Xu, T. C. Sum, *Adv. Mater.* **2019**, *31*, 1802486.

[34] I. Minda, J. Horn, E. Ahmed, D. Schlettwein, H. Schwoerer, *ChemPhysChem* **2018**, *19*, 3010.

[35] I. A. Alfurayj, Z. Li, C. Burda, *J. Phys. Chem. C* **2021**, *125*, 15113.

[36] T. Wu, R. Zhao, J. Qiu, S. Wang, X. Zhang, Y. Hua, *Adv. Funct. Mater.* **2022**, *32*, 2204450.

[37] P. Chen, Y. Xiao, L. Li, L. Zhao, M. Yu, S. Li, J. Hu, B. Liu, Y. Yang, D. Luo, C.-H. Hou, X. Guo, J.-J. Shyue, Z.-H. Lu, Q. Gong, H. J. Snaith, R. Zhu, *Adv. Mater.* **2023**, *35*, 2206345.

[38] Y. Shao, Z. Xiao, C. Bi, Y. Yuan, J. Huang, *Nat. Commun.* **2014**, *5*, 5784.

[39] G. Xing, N. Mathews, S. S. Lim, N. Yantara, X. Liu, D. Sabba, M. Grätzel, S. Mhaisalkar, T. C. Sum, *Nat. Mater.* **2014**, *13*, 476.

[40] W. Li, W. Zhang, S. Van Reenen, R. J. Sutton, J. Fan, A. A. Haghighirad, M. B. Johnston, L. Wang, H. J. Snaith, *Energy Environ. Sci.* **2016**, *9*, 490.

[41] Z. Ni, H. Jiao, C. Fei, H. Gu, S. Xu, Z. Yu, G. Yang, Y. Deng, Q. Jiang, Y. Liu, Y. Yan, J. Huang, *Nat. Energy* **2022**, *7*, 65.

[42] K. Chen, P. Wu, W. Yang, R. Su, D. Luo, X. Yang, Y. Tu, R. Zhu, Q. Gong, *Nano Energy* **2018**, *49*, 411.

[43] M. Li, S. Bhaumik, T. W. Goh, M. S. Kumar, N. Yantara, M. Grätzel, S. Mhaisalkar, N. Mathews, T. C. Sum, *Nat. Commun.* **2017**, *8*, 14350.

[44] R. Su, Z. Xu, J. Wu, D. Luo, Q. Hu, W. Yang, X. Yang, R. Zhang, H. Yu, T. P. Russell, Q. Gong, W. Zhang, R. Zhu, *Nat. Commun.* **2021**, *12*, 2479.

[45] S. Mahesh, J. M. Ball, R. D. Oliver, D. P. McMeekin, P. K. Nayak, M. B. Johnston, H. J. Snaith, *Energy Environ. Sci.* **2020**, *13*, 258.

[46] D. Luo, W. Yang, Z. Wang, A. Sadhanala, Q. Hu, R. Su, R. Shivanna, G. F. Trindade, J. F. Watts, Z. Xu, T. Liu, K. Chen, F. Ye, P. Wu, L. Zhao, J. Wu, Y. Tu, Y. Zhang, X. Yang, W. Zhang, R. H. Friend, Q. Gong, H. J. Snaith, R. Zhu, *Science* **2018**, *360*, 1442.

[47] X. Ling, S. Zhou, J. Yuan, J. Shi, Y. Qian, B. W. Larson, Q. Zhao, C. Qin, F. Li, G. Shi, C. Stewart, J. Hu, X. Zhang, J. M. Luther, S. Duhm, W. Ma, *Adv. Energy Mater.* **2019**, *9*, 1900721.

[48] T. Kim, W. Kim, O. Vakuliuk, D. T. Gryko, D. Kim, *J. Am. Chem. Soc.* **2019**, *142*, 1564.

[49] W. Kim, T. Kim, S. Kang, Y. Hong, F. Würthner, D. Kim, *Angew. Chem., Int. Ed.* **2020**, *59*, 8571.

[50] Y. Y. Kim, J. Kim, N. Kim, Zenodo **2022**, 10.5281/zenodo.7042272.